galaxies

MDPI

Article

ALMA Observations of G333.6-0.2: Molecular and Ionized Gas Environment

Aruzhan Omar [1,2], Aidana Abdirakhman [1,*], Nazgul Alimgazinova [1,2,*], Meiramgul Kyzgarina [1,2], Aisha Naurzbayeva [1,2], Zhomartkali Islyam [1], Kunduz Turekhanova [1,2], Aizat Demessinova [1,2] and Arailym Manapbayeva [2]

[1] Faculty of Physics and Technology, Al-Farabi Kazakh National University, Al-Farabi Ave., 71, Almaty 050040, Kazakhstan; omaruzhan@gmail.com (A.O.)
[2] Institute of Experimental and Theoretical Physics, Al-Farabi Kazakh National University, Almaty 050040, Kazakhstan
* Correspondence: armiyaqyzyaidana@gmail.com (A.A.); nukosi1305@gmail.com (N.A.)

Abstract

We present high-angular resolution observations, conducted with the Atacama Large Millimeter/Submillimeter Array (ALMA) in Band 6, of high-excitation molecular lines of CH_3CN, CH_3OH, and the H29α radio recombination line, towards the G333.6-0.2 ultracompact (UC) H II region. Our observations reveal three hot molecular cores: A, B, and C, where emission is detected in ten components of the $J = 14 \rightarrow 13$ rotational ladder of CH_3CN and in the CH_3OH $J = 5_{1,4} \rightarrow 4_{1,3}$ transition. Rotational diagram analysis of CH_3CN reveals excitation temperatures ranging from 380 to 430 K. First-order moment maps of CH_3CN and CH_3OH reveal distinct velocity gradients in all cores, suggesting rotating structures, with core A also showing evidence of expansion motions. The H29α recombination line shows a linewidth of 30.2 $\pm$ 0.12 km s^{-1}, dominated by dynamical and thermal broadening, indicative of large-scale motions in ionized gas. Analysis of the ionized gas properties yields an electron density of $(4.8 \pm 0.4) \times 10^5$ cm^{-3}, an emission measure of $(1.23 \pm 0.06) \times 10^9$ pc cm^{-6}, and a Lyman continuum photon flux consistent with an O5–O6 V (Zero-Age Main Sequence; ZAMS) star. Our results suggest that G333.6-0.2 is in an intermediate evolutionary stage between hypercompact (HC) and ultracompact (UC) H II regions, hosting active high-mass star formation with rotating hot cores and ionized gas dynamics.

Keywords: H II regions; individual object (G333.6-0.2); star formation; massive stars; hot molecular cores; molecular gas; ionized gas

check for updates

Academic Editor: Jorick S. Vink

Received: 26 March 2025
Revised: 19 June 2025
Accepted: 24 June 2025
Published: 27 June 2025

Citation: Omar, A.; Abdirakhman, A.; Alimgazinova, N.; Kyzgarina, M.; Naurzbayeva, A.; Islyam, Z.; Turekhanova, K.; Demessinova, A.; Manapbayeva, A. ALMA Observations of G333.6-0.2: Molecular and Ionized Gas Environment. *Galaxies* **2025**, *13*, 73. https://doi.org/10.3390/galaxies13040073

1. Introduction

High-mass star-forming regions (HMSFRs) exhibit rich chemistry that significantly influences the evolution and composition of the interstellar medium (ISM) [1]. Over the years, numerous complex organic molecules (COMs) have been identified in hot molecular cores [2], which are compact, hot, and dense regions associated with luminous infrared (IR) sources or UC H II regions [3,4].

Various complex physical processes, including accretion, infall, and outflows, occur during the early evolutionary stages of HMSFRs. They begin within dense and massive molecular cores, where high-mass protostellar objects accrete material at rates of 10^{-5} to 10^{-3} $M_\odot$ yr^{-1} [1]. These objects complete their Kelvin–Helmholtz (K–H) contraction rapidly and transition to the main sequence [5]. At this stage, the star emits extreme ultraviolet (UV) photons, ionizing its surroundings and creating compact regions of ionized gas. Observationally, these regions are characterized by sizes (r) $\leq$ 0.03 pc, densities (n_e) $> 10^6$ cm^{-3}, and emission measures (EM) exceeding 10^8 pc cm^{-6} [6].

The object of our study, G333.6-0.2, is a bright H II region extensively observed at radio and infrared wavelengths [7,8], but completely obscured at optical wavelengths. This region is located at a distance of approximately 3.1–3.6 kpc from the Sun [8–10] and is thought to be ionized by a cluster of massive O–B type stars [11].

G333.6-0.2 is classified as an UC H II region [12], embedded within the giant H II complex RCW 106 [13]. Its total luminosity is estimated to be less than $9.0 \times 10^5, L_\odot$ [9], indicating ongoing high-mass star formation. Based on radio continuum analysis, G333.6-0.2 is suggested to harbor the equivalent of 19 O7V-type stars [8]. However, it has also been argued that the ionizing sources may include even earlier spectral types, ranging from O3 to O5 [9].

In this work, we present high-angular resolution interferometric observations (ALMA archival data) toward G333.6-0.2. We report the detection of high-excitation lines of CH_3CN and CH_3OH, as well as the H29α radio recombination line, and analyze the kinematics and physical properties of the hot molecular cores associated with this UC H II region. In Section 2, we describe the observations and data reduction process. Section 3 presents the analysis of the molecular gas environment. In Section 4, we analyze the rotational diagrams to derive physical parameters. Section 5 focuses on radio recombination line (RRL) fitting and the estimation of broadening parameters. In Section 6, we discuss the derived properties of the H II region. Finally, all results are summarized in Section 7.

2. Observations

We analyze archival ALMA data (Project 2016.1.00577.S) covering the 240.8 to 260.625 GHz frequency range (Band 6) to investigate molecular line emission towards the UC H,II region G333.6-0.2. Observations were conducted in August 2017 using forty 12 m antennas. The array configuration provided baseline lengths ranging from 108.440 m to 864.182 m, resulting in a synthesized beam size of 0″163. The observations covered four spectral windows spanning the frequency ranges 240.82–241.288 GHz, 243.72–244.188 GHz, 256.119–256.587 GHz, and 257.156–257.625 GHz. The phase center of the array was set to $\alpha_{J2000} = 16^h22^m09^s, \delta_{J2000} = -50°15'59''$. The flux calibrator was Titan, the phase calibrator was J1427-4206 and the bandpass calibrator was J1603-4904. The data cube has a spectral resolution of 488 kHz and a synthesized beam of 0″23×0″.14 with a position angle (PA) of $\sim -41.9°$. The systemic velocity of the source is known to be ~ -47 km s^{-1}. Image analysis was performed using the CASA 4.7.2 software package [14]. Spectral line identification and processing analysis presented in this article were performed using the software packages CASA, CARTA, and MADCUBA, while final visualization was performed using AstroPy [15].

3. Molecular Gas Environment

The molecular gas environment surrounding the G333.6-0.2 UC H II region has been analyzed using high-resolution ALMA observations. We present the results obtained for typical hot core tracers, such as CH_3CN , $CH_3^{13}CN$, and CH_3OH.

Based on the analysis of moment maps and spectral profiles, we identified three cores around the G333.6-0.2 H II region. Cores A and C are identified as hot core candidates based on the detection of CH_3OCHO lines at 216.1 GHz [16]. From the G333.6-0.2 H II region, core A is located at a distance of 0.29 pc, core B at 0.25 pc, and core C at 0.33 pc, assuming a distance of 4.2 kpc [17,18].

Figure 1 presents the moment 0 map of CH_3CN emission shown in color scale, with the moment 0 contours of the H29 α recombination line overlaid in gray. Three distinct molecular cores are identified in the CH_3CN emission map and are labeled as A-core, B-core, and C-core. Three distinct molecular cores are identified in the CH_3CN emission map and are labeled as A-core, B-core, and C-core. We estimate the size of the emission regions by fitting a two-dimensional Gaussian. We also estimate the deconvolved source sizes using the following formula:

$$\text{Source Size} = \sqrt{\text{FWHM}_{\text{maj}} \times \text{FWHM}_{\text{min}} - \theta_{\text{beam}}^2},$$

where FWHM_{maj} and FWHM_{min} are the major and minor FWHM size obtained from the two-dimensional Gaussian fit, and θ_{beam} is the geometric mean of the beam's major and minor axes, calculated as

$$\theta_{\text{beam}} = \sqrt{b_{\text{maj}} \times b_{\text{min}}}.$$

The sizes and coordinates of the cores, along with the peak velocities of the molecular lines, are listed in Table 1. These molecular cores are spatially separated and exhibit different peak intensities, with A-core being the brightest. A zoomed-in view and further characterization of each core are provided in the corresponding moment maps.

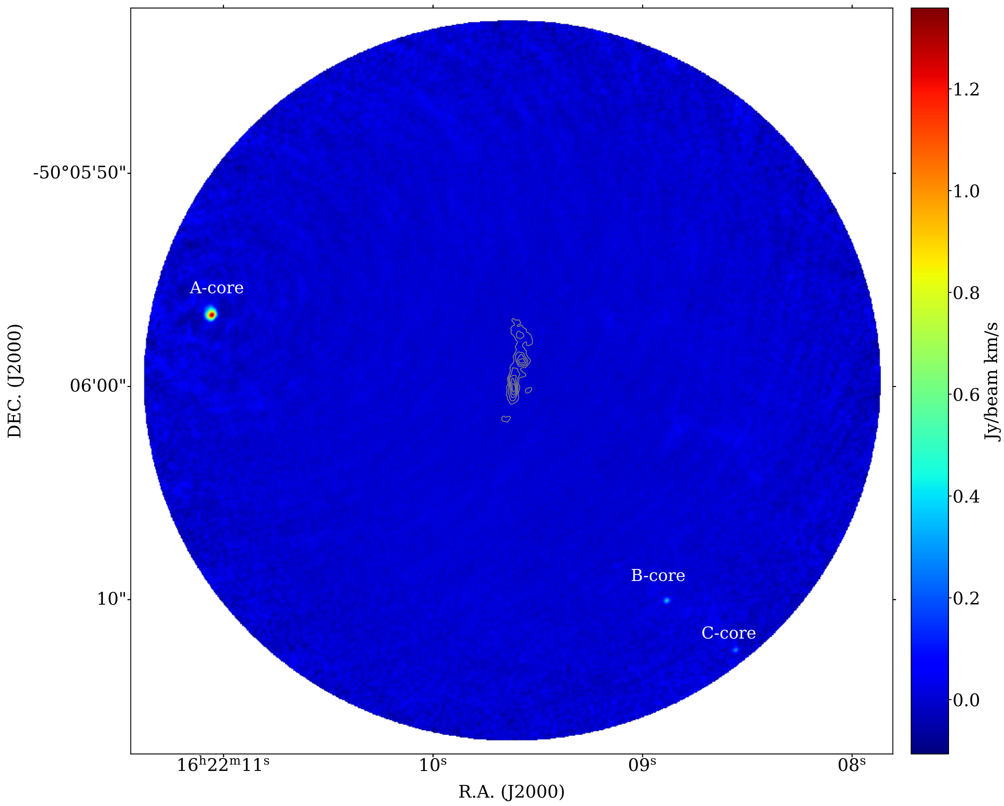

Figure 1. Moment 0 map of CH_3CN emission (color scale) overlaid with H29α moment 0 contours. Three molecular cores labeled A, B, and C.

Figure 2 shows the emission spectrum of the $J = 14 \rightarrow 13$ rotational transition of CH_3CN, integrated over a region corresponding to a beam diameter. Other molecular lines are also present.

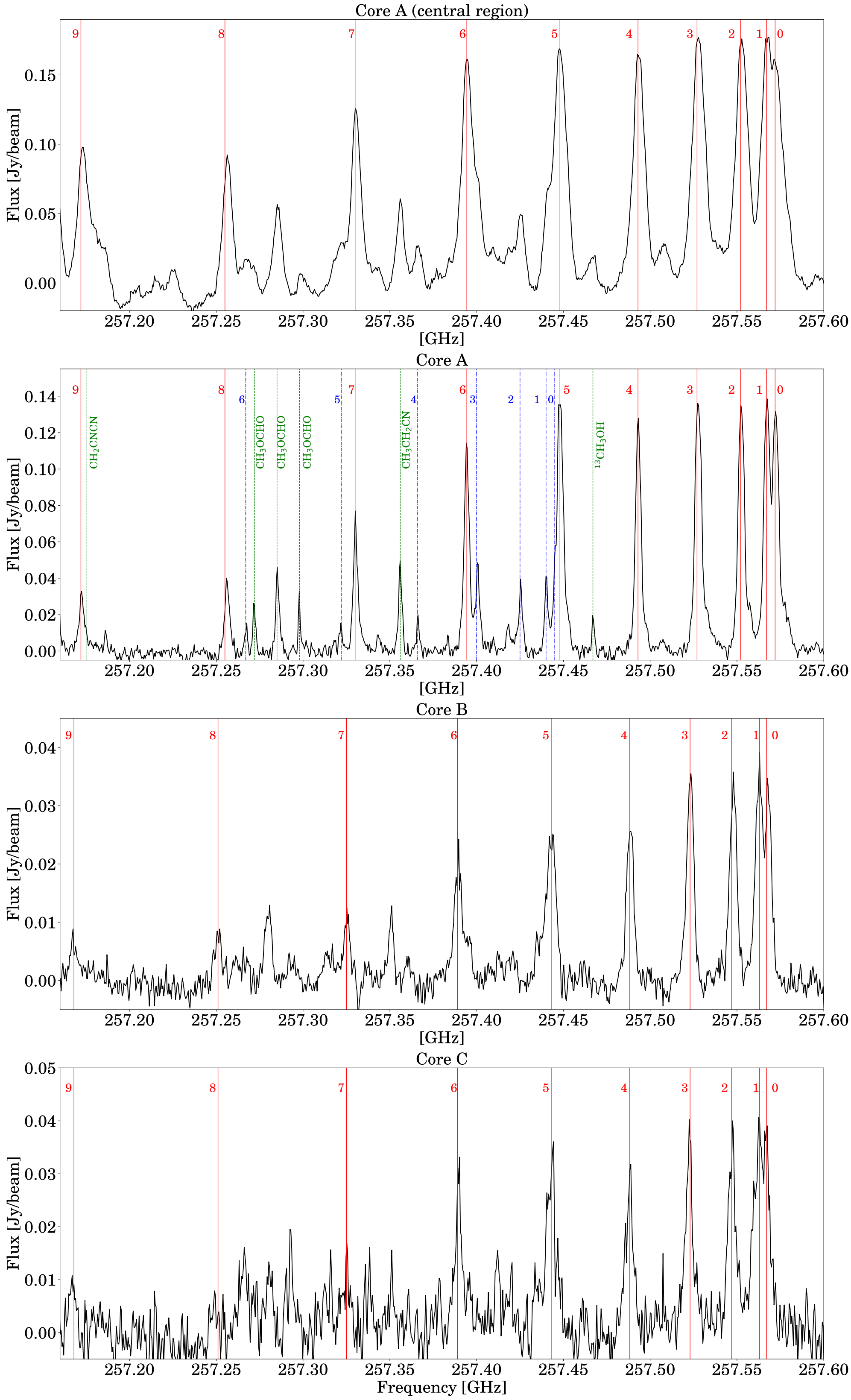

Figure 2. Spectra of CH_3CN emission in the $J = 14 \rightarrow 13$ transition. (**Top**) Core A (central region); (**Second**) core A; (**Third**) core B; (**Bottom**) core C. The K-components (K = 0–9) are marked with red dashed lines ($V_{LSR} = -47$ km s^{-1}). Additional molecular lines detected in core A are marked with blue dashed lines.

Table 1. Coordinates, peak velocities, and sizes of the hot cores.

Core	Coordinates (RA, Dec)	V_{LSR} [km s^{-1}]	Size^a [$''$]	Size$^b_{deconv}$ [$''$]
A	($16^h\ 22^m\ 11.061^s$, $-50°05'56''64$)	-52.3	0.360	0.315
B	($16^h\ 22^m\ 08.892^s$, $-50°06'10''03$)	-46.9	0.237	0.162
C	($16^h\ 22^m\ 08.559^s$, $-50°06'12''34$)	-46.2	0.247	0.176

[a] Observed source size from a 2D Gaussian fit (FWHM, not deconvolved). [b] Deconvolved source size, corrected for beam broadening using the geometric mean beam size.

We detected the emission of CH_3CN in three cores, identified as A, B, and C. The ten components ($K = 0, 1, \ldots, 9$) of the $J = 14 \rightarrow 13$ ladder of CH_3CN are detected in these cores. For core A, the spectra were extracted from a region located northeast of the center (indicated by a blue plus sign), while the central region exhibits saturation and significant line blending (see Figure 3).

In addition, seven components ($K = 0$ to $K = 6$) of the $J = 14 \rightarrow 13$ transition of the $CH_3^{13}CN$ molecule were identified (indicated by blue dash-dot lines). Other molecular species identified within this spectral window are marked in green and Table 2 lists the identified transitions, line frequencies, and upper-state energy levels for the three cores.

Table 2. Observational parameters of CH_3CN $J = 14 \rightarrow 13$ rotational transitions and other detected lines within this spectral window.

Species	Transition	Frequency (GHz)	E_u/k (K)
CH_3CN	$14_0 \rightarrow 13_0$	257.527	92.70
	$14_1 \rightarrow 13_1$	257.522	99.85
	$14_2 \rightarrow 13_2$	257.508	121.28
	$14_3 \rightarrow 13_3$	257.483	156.99
	$14_4 \rightarrow 13_4$	257.448	206.98
	$14_5 \rightarrow 13_5$	257.404	271.23
	$14_6 \rightarrow 13_6$	257.349	349.72
	$14_7 \rightarrow 13_7$	257.285	442.45
	$14_8 \rightarrow 13_8$	257.210	549.38
	$14_9 \rightarrow 13_9$	257.127	670.50
$CH_3{}^{13}CN$	$14_0 \rightarrow 13_0$, F = 14-13	257.400	92.65
	$14_1 \rightarrow 13_1$, F = 14-13	257.395	99.80
	$14_2 \rightarrow 13_2$, F = 14-13	257.380	121.23
	$14_3 \rightarrow 13_3$, F = 14-13	257.355	156.94
	$14_4 \rightarrow 13_4$, F = 14-13	257.321	206.93
	$14_5 \rightarrow 13_5$, F = 14-13	257.276	271.17
	$14_6 \rightarrow 13_6$, F = 14-13	257.222	349.67
CH_3OCHO	23 (2.22)−22 (2.21) E	257.242	342.23
	20 (5.15)–19 (5.14) E	257.227	142.79
	20 (5.15)–19 (5.14) A	257.253	142.79
$^{13}CH_3OH$	15 (3.13)–15 (2.14)	257.422	321.79
CH_3CH_2CN	30 (0.30)–29 (0.29)	257.310	193.54
CH_2CHCN	27 (16.11)–26 (16.10)	257.130	1718.76

Note: The letters "A" and "E" refer to torsional species of the CH_3 group caused by internal rotation. These symmetry labels arise from the quantum mechanical treatment of the hindered rotation of the methyl group in asymmetric top molecules such as CH_3OCHO.

Figure 3 shows the moment maps of the CH_3CN $J = 14 \rightarrow 13$, $K = 2$ transition for cores A (left panels), B (middle panels), and C (right panels). For core A, the zero-order moment map shows a brightness increasing from the edge toward the center, reaching approximately 1.2 Jy beam $^{-1}$ km s^{-1}. The first-order moment map shows that the molecular gas exhibits two distinct velocity gradients: one from southwest (SW) to northeast (NE), suggesting gas expansion, and another from southeast (SE) to northwest (NW), indicative of rotational motion [19,20]. The second-order moment map (bottom panel) displays a velocity dispersion reaching up to ∼25 km^2 s^{-2}, which may be related to line saturation. For core B, the brightness in the zero-order moment map is ∼0.4 Jy beam $^{-1}$ km s^{-1}. The first-order moment map shows a velocity gradient oriented from southeast to northwest. For core C, the zero-order moment map displays a brightness of ∼0.25 Jy beam $^{-1}$ km s^{-1} and the first-order moment map reveals a velocity gradient directed from west to east. The average velocity for both cores is approximately -46 km s^{-1}. The second order moment map indicates a velocity dispersion of about 5 km^2 s^{-2} for both cores.The velocity gradients observed in the first-order moment maps suggest the presence of ordered rotational kinematics.

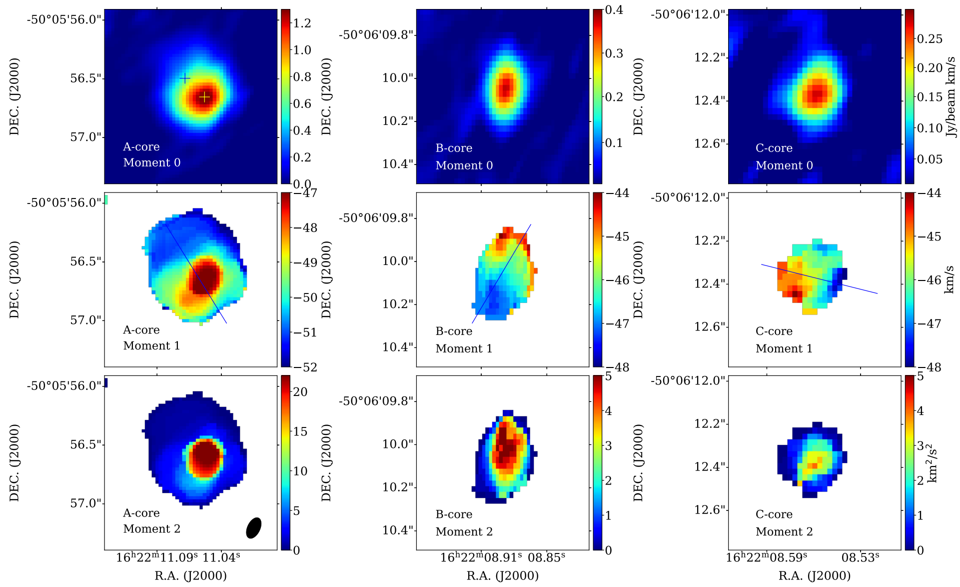

Figure 3. Images of the velocity-integrated intensity (moment 0; **upper panels**), intensity-weighted velocities (moment 1; **middle panels**), and velocity dispersion map (moment 2; **lower panels**) in the CH_3CN $J = 14 \rightarrow 13$ K = 2 transition for cores A, B, C. The black ellipse shown at the bottom right corner of the lower left panel indicates the beam size.

The spectral emission of the CH_3OH molecule for cores A, B, and C is shown in Figure 4. The molecular line corresponds to a frequency of 243.916 GHz with a transition $J = 5_{1,4} \rightarrow 4_{1,3}$. To compare the results obtained for molecular gas, we analyzed the moment maps (see Figure 5) of CH_3OH emission for the A, B, and C cores.

Figure 5 shows the moment maps (Moment 0, 1, and 2) of CH_3OH emission toward cores A, B, and C. For core A, the zero-order moment map (top panel) shows a centrally peaked brightness distribution, reaching up to ∼0.25 Jy beam^{-1} km s^{-1}. The first-order moment map (middle panel) reveals a velocity gradient oriented from southeast (SE) to northwest (NW), indicative of ordered gas motions. The second-order moment map (bottom panel) displays a velocity dispersion up to ∼3.0 km^2 s^{-2}.

For core B, the CH_3OH zero-order moment map (top panel) shows lower brightness compared to core A, with an integrated intensity of ∼0.15 Jy beam^{-1} km s^{-1}. The velocity gradient seen in the first-order moment map (middle panel) is directed from south to north. The second-order moment map (bottom panel) indicates a velocity dispersion of up to ∼2.0 km^2 s^{-2}.

For core C, the zero-order moment map (top panel) exhibits a peak intensity of $\sim$0.10 Jy beam^{-1} km s^{-1}. The first-order moment map (middle panel) shows a velocity gradient extending from southwest to northeast. The velocity dispersion shown in the second-order moment map (bottom panel) reaches $\sim$1.5 km^2 s^{-2}.

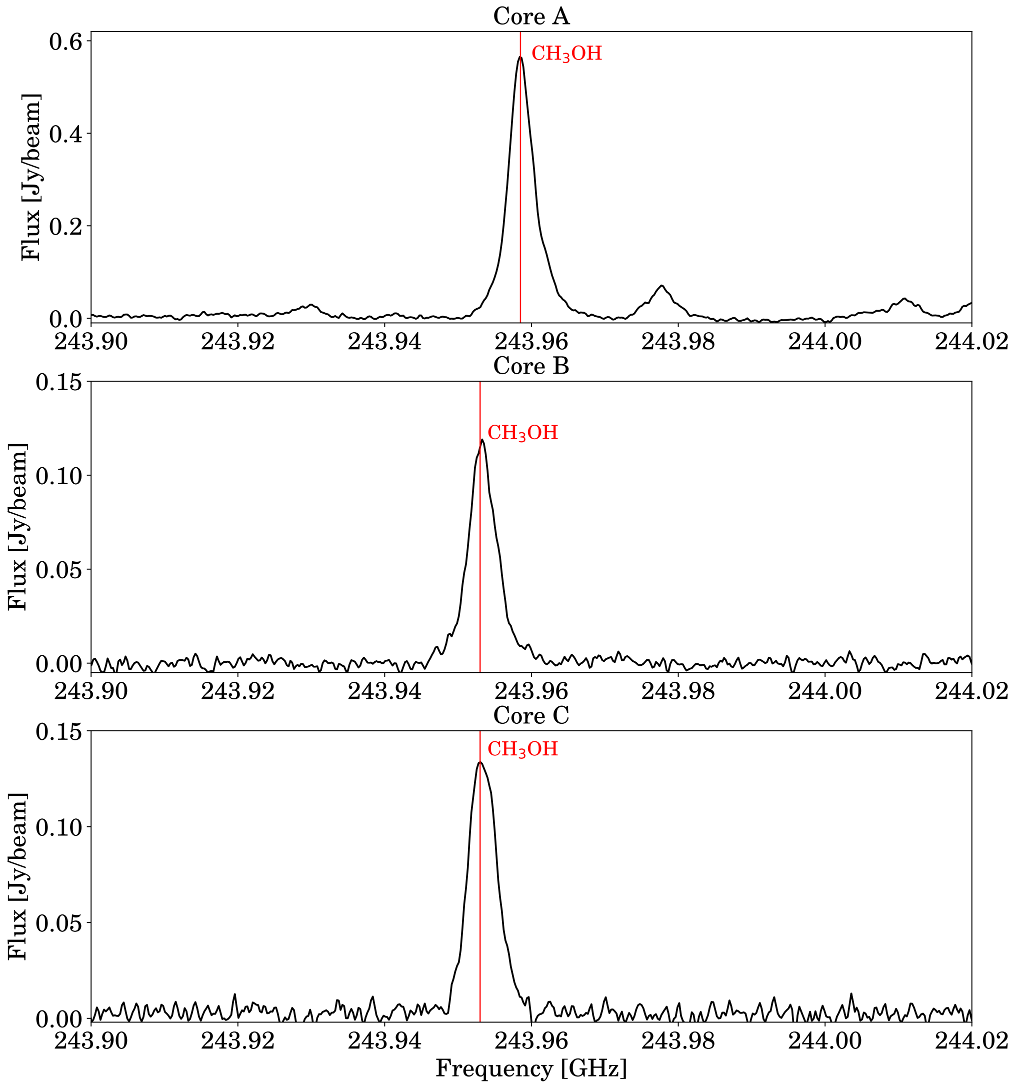

Figure 4. Spectral emission features of CH_3OH toward cores A, B, and C. The red line shows the detected CH_3OH spectrum.

These velocity gradients observed in the first-order moment maps suggest the presence of organized gas motions within the molecular cores.

In Figure 6, the position–velocity (PV) diagrams for the three core structures are presented. PV cuts were extracted along the axes of the local velocity gradients, as identified from the moment 1 (intensity-weighted velocity) maps (see Figure 3). The PV axes are overlaid on the moment 1 images for reference. The velocity gradient in core A is oriented from northeast to southwest (position angle 30°); in core B, from southeast to northwest (PA −45°); and in core C, from northeast to southwest (PA 78°).

The position–velocity (PV) diagram of core A reveals an asymmetric velocity structure. The redshifted side shows a butterfly-like pattern indicative of Keplerian-like rotation, whereas the blueshifted side is less prominent.

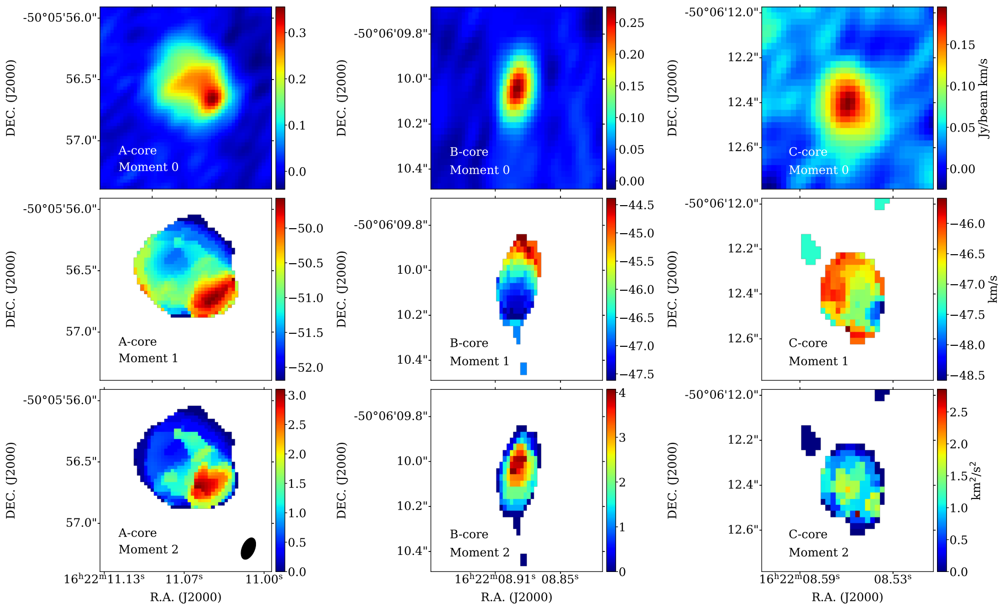

Figure 5. Same as Figure 5 for CH_3OH $J = 5_{1,4}$–$4_{1,3}$ emission.

In contrast, the PV diagrams of cores B and C exhibit more symmetric velocity gradients on both sides of the central position. These features are consistent with rotational motion within the molecular cores, though without clear signatures of Keplerian dynamics. The observed kinematics suggest that cores B and C are rotating structures, potentially in earlier or less compact evolutionary stages than core A.

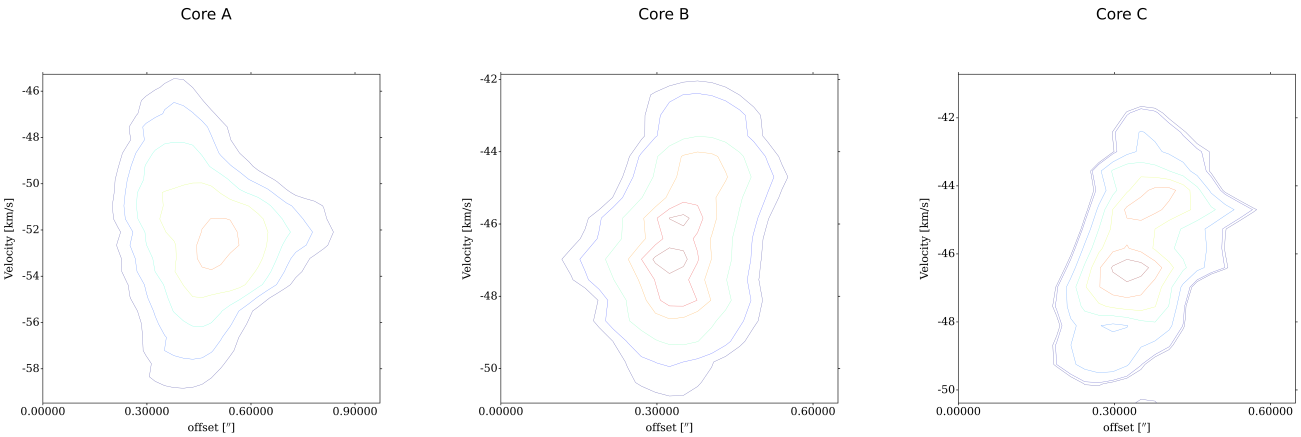

Figure 6. Position–velocity (PV) diagrams of cores A, B, and C. The color scale represents the emission intensity in Jy beam^{-1} for each core. For core A, the intensity ranges from 0.075 to 0.2 Jy beam^{-1}; for core B, from 0.015 to 0.048 Jy beam^{-1}; and for core C, from 0.014 to 0.04 Jy beam^{-1}.

4. Rotation Diagram Analysis: Estimation of Gas Temperature

We employed rotation diagram analysis to derive the rotational temperatures. We performed the derivation of the rotational temperature and total column density of CH_3CN using the Madrid Data Cube Analysis (`MADCUBA`) software, assuming local thermodynamic equilibrium (LTE) [21].

Figure 7 shows the rotational diagrams of the cores A and B. The derived rotational temperatures for cores A and B are 430 $\pm$ 65 K and 383 $\pm$ 46 K, respectively, with corresponding column densities of 2.24×10^{12} cm^{-2} and 7.94×10^{12} cm^{-2}.

The data points corresponding to energy levels of 271 K (K = 5) and 670 K (K = 9) were excluded from the fit. This is because the K = 5 component of methyl cyanide overlaps with the K = 0 transition of $CH_3^{13}CN$, while the K = 9 transition at 670 K is blended with a line from CH_2CHCN.

In addition, the rotational temperature and column density were also derived for core A using the $CH_3^{13}CN$ isotopologue. These values were obtained based on seven detected components ($K = 0$ to $K = 6$) of the $J = 14 \rightarrow 13$ transition. The resulting temperature is 140 ± 14 K, and the corresponding column density is 3.44×10^{11} cm^{-2}.

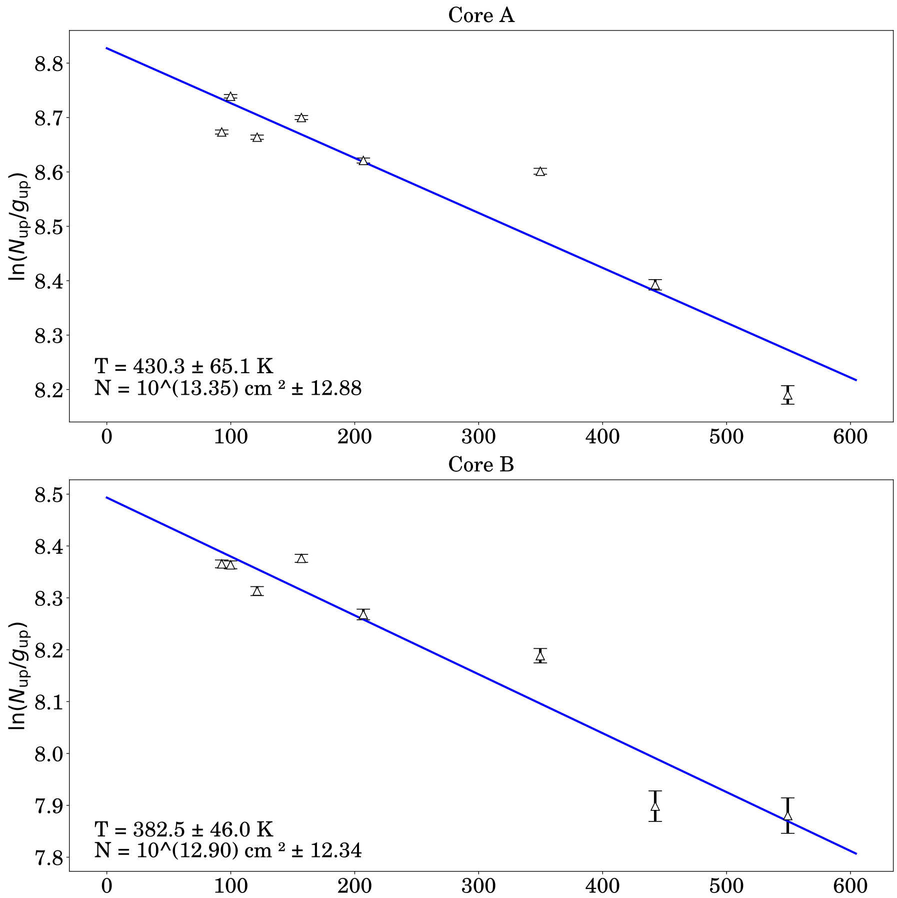

Figure 7. Rotational diagrams of cores A and B. The black open triangles represent the observed data points of CH_3CN rotational transitions, and the solid blue lines indicate the best-fit linear regressions used to estimate the excitation temperature and column density.

5. Radio Recombination Lines: H29*α* and He29*α*

We identified the radio recombination lines (RRLs): H29*α* (256.302 GHz) and He29*α* (256.317 GHz). Figure 7 shows the spectrum of the H29*α* and He29*α* recombination lines, integrated over the peak position (0.26″) of the recombination emission indicated by the white cross in Figure 8. A Gaussian fit to the H29*α* line profile yields a linewidth (FWHM) of 30.2 $\pm$ 0.12 km s^{-1} and a central velocity of $V_{LSR} = -40.57 \pm 0.05$ km s^{-1}, a peak amplitude of 0.418 ± 0.001 Jy.

For the He29*α* line, the fitted linewidth (FWHM) is 28.57 $\pm$ 1.23 km s^{-1}, with a central velocity of $V_{LSR} = -37.52 \pm 0.5$ km s^{-1}, and a peak amplitude of 0.0399 ± 0.0015 Jy. A Gaussian fit to the He29*α* line profile yields a full width at half maximum (FWHM) of 17.41 ± 0.43 km s^{-1}, a central velocity of $V_{LSR} = -37.52 \pm 0.18$ km s^{-1}, and a peak amplitude of 0.00887 ± 0.00019 Jy. The corresponding integrated intensity is measured to be 0.164 ± 0.004 Jy km s^{-1}. Notably, the central velocities of the recombination lines differ from those of the molecular lines, which may indicate a slight spatial offset between the ionized gas and the molecular material [22]. As an initial estimate for the relative He-to-H line brightness, we calculate a helium-to-hydrogen number abundance of $N_{\mathrm{He}}/N_{\mathrm{H}} = 0.09 \pm 0.005$ [23]. This value is typical for the interstellar medium (ISM) in the Milky Way [24].

Figure 9 presents the velocity-integrated intensity (moment 0) and intensity-weighted velocity (moment 1) maps of the H29α line. The integration was performed over the velocity range $-73\,\mathrm{km\,s^{-1}}$ to $-5\,\mathrm{km\,s^{-1}}$. The position of the peak emission in the velocity-integrated map, marked with a white cross, reaches a maximum intensity of $3\,\mathrm{Jy\,beam^{-1}\,km\,s^{-1}}$. The moment 1 map reveals a clear velocity gradient from northwest to southeast, suggesting rotational motion or an outflow/infall.

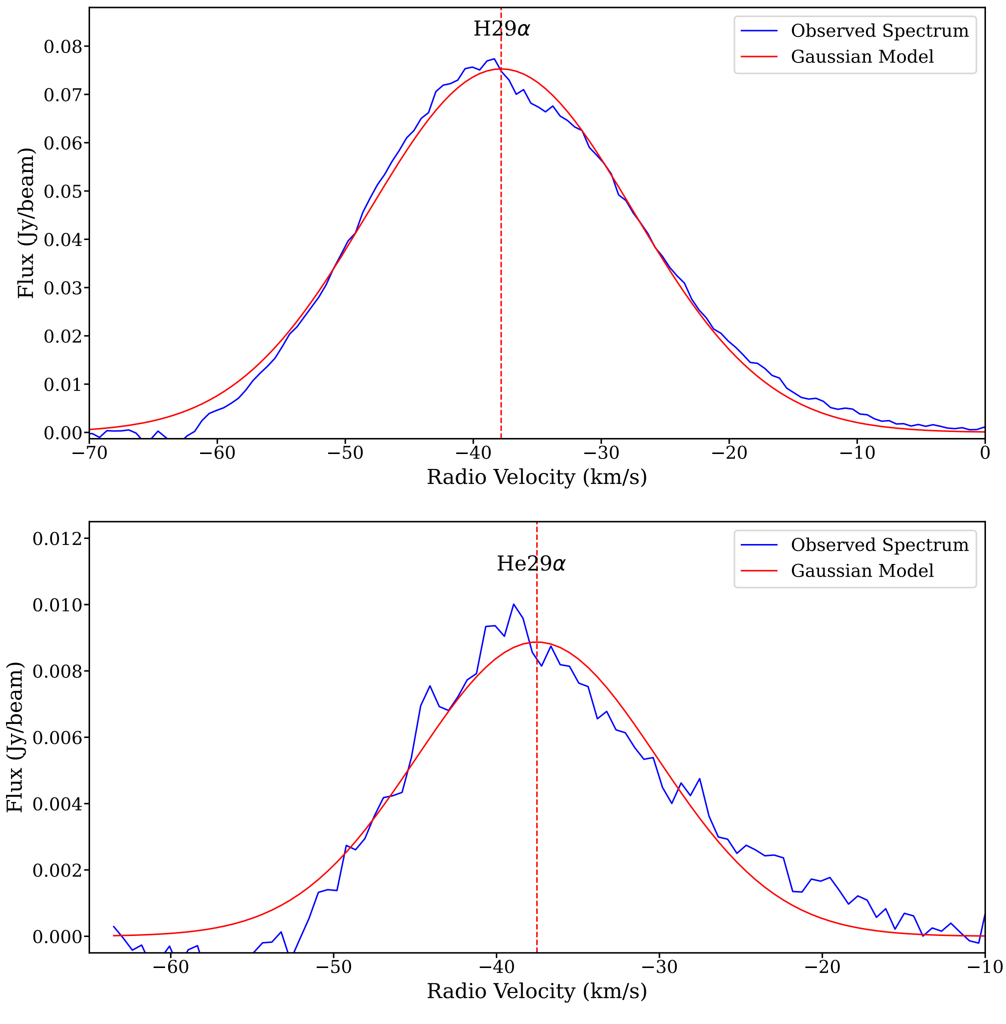

Figure 8. Spectrum of the H29α and He29α radio recombination lines (RRLs). The blue line indicates the observed data and the red line denotes the Gaussian model fit.

The observed linewidth (ΔV) of the H29α radio recombination line is determined by a combination of pressure broadening (ΔV_{P}) and Doppler broadening (ΔV_{D}). The Doppler broadening itself consists of two components: thermal broadening (ΔV_{ther}), caused by the thermal motion of particles and dynamical broadening (ΔV_{dyn}), which arises from large-scale motions such as infall, outflow, or rotation. Thus, the total observed linewidth can be expressed as the quadrature sum of these contributions. The line broadening mechanisms can be described as follows [25]:

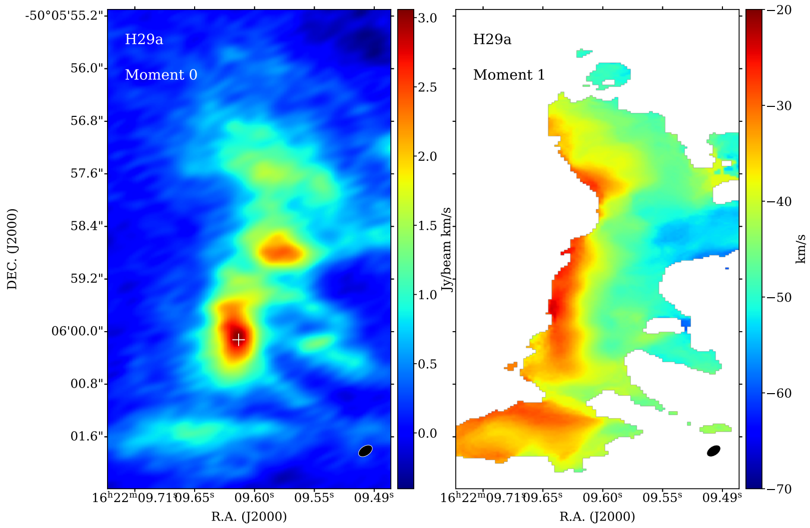

Figure 9. Maps of the velocity-integrated intensity (moment 0; **left panel**) and intensity-weighted velocity (moment 1; **right panel**) of the H29α radio recombination line. The black ellipse at the bottom right corner indicates the synthesized beam. The white plus sign marks the peak of RRL emission at RA = $16^h22^m09.617^s$, Dec = $-50°06'00''110$.

$$\Delta V = \sqrt{\Delta V_{\rm D}^2 + \Delta V_{\rm P}^2} \tag{1}$$

$$\Delta V_D = \sqrt{\Delta V_{\rm dyn}^2 + \Delta V_{\rm ther}^2} = \sqrt{\Delta V_{\rm dyn} + 0.0458(T_e)} \tag{2}$$

$$\Delta V_{\rm P} = 3.74 \times 10^{-14} \times n^{4.4} \times n_{\rm e} \times \lambda \times T_{\rm e}^{-0.1}, \tag{3}$$

where n = 29 is the principal quantum number of the H29α. The line broadening is estimated using the local electron density and electron temperature for the UC H II region. The thermal broadening is $\Delta V_{\rm ther} \approx 19.56$ km s^{-1}. The pressure broadening is $\Delta V_P \approx 0.02$ km s^{-1} and contributes little to the total linewidth. The dynamical broadening is $\Delta V_{\rm dyn} \approx 23.01$ km s^{-1}. Dynamical broadening dominates, indicating contributions from large-scale motions; this is further supported by intensity-weighted velocity (moment 1) maps of the H29α line.

6. Properties of the H II Region

We use the size $\theta_s = \sqrt{0''29 \times 0''23} \approx 0''26$ of the maximum peak, indicated by the white cross (see Figure 9), to calculate the parameters of the ionized gas. The emission measure (EM) is a crucial parameter for the H II region. We derive EM using the equation from [26–28]:

$$\mathrm{EM} = 7.1\,\mathrm{pc\,cm}^{-6} \left(\frac{S_L}{\mathrm{Jy}}\right) \left(\frac{\lambda}{\mathrm{mm}}\right) \left(\frac{T_e}{\mathrm{K}}\right)^{1.5} \left(\frac{\Delta V}{\mathrm{km\,s}^{-1}}\right) \left(\frac{\theta_s}{\mathrm{arcsec}}\right)^{-2} \tag{4}$$

We used electron temperature T_e = 8350 K from [12]. For the H29α line, the peak line intensity is S_L = 0.42 Jy. Based on the parameters above, we calculated an EM = $(1.23 \pm 0.006) \times 10^9$ pc cm^{-6}. The corresponding volume electron density is obtained $n_e = (4.8 \pm 0.4) \times 10^5$ cm^{-3} from EM $= n_e^2 L f_v$ where $L = 4.2\,\mathrm{kpc} \times \tan(0''26) = 0.0053$ pc = 1092 AU is the path length and f_V = 1 is a volume filling factor. We employ a mass of H II region, the Lyman continuum photon number (N_L), and the excitation parameter (U) to infer the corresponding star type. The corresponding equations are expressed [29–31].

$$\frac{M_{\rm HII}}{M_\odot} = 3.7 \times 10^{-5} \left(\frac{\nu}{\rm GHz}\right)^{0.05} \left(\frac{S_\nu}{\rm mJy}\right)^{0.5} \left(\frac{T_e}{10^4 \rm K}\right)^{0.175} \left(\frac{\theta_s}{\rm arcsec}\right)^{1.5} \left(\frac{D}{\rm kpc}\right)^{2.5} \quad (5)$$

$$\mathrm{N_L} = 4.761 \times 10^{48} \mathrm{s}^{-1} \alpha(\nu, T_e)^{-1} \left(\frac{\nu}{\rm GHz}\right)^{0.1} \left(\frac{D}{\rm kpc}\right)^{2} \left(\frac{S_\nu}{\rm Jy}\right) \left(\frac{T_e}{\rm K}\right)^{-0.45} \quad (6)$$

$$\mathrm{U} = 2.706 \times 10^{-16} \mathrm{pc\,cm^{-2}} \left(\frac{T_e}{\rm K}\right)^{4/15} \left(\frac{\mathrm{N_L}}{\mathrm{s^{-1}}}\right)^{1/3} \quad (7)$$

where D = 4.2 $\pm$ 0.7 kpc is the source distance, $\alpha(\nu, T_e)$ $\sim$1 is a slowly varying function [30,32]. We used continuum flux density (S_ν) at 250 GHz [13]. Based on our previously obtained parameters, we get a mass of ionized gas $M_{\rm HII} = (3.9 \pm 2.5) \times 10^{-2} M_\odot$ and $N_L = (7.5 \pm 2.5) \times 10^{49}$ s^{-1}, $U = 126.6 \pm 14\,\mathrm{pc\,cm^{-2}}$. The estimated Lyman continuum photon flux suggests the presence of a massive star with a spectral type of O5-O6 V (ZAMS) [33]. The physical parameters of the H II region indicate an intermediate evolutionary stage between hypercompact (HC) and ultracompact (UC) H II regions [34].

7. Conclusions

We have reported high-angular resolution ALMA Band 6 observations of highly excited molecular lines of CH_3CN and CH_3OH, along with the H29α radio recombination line, toward the UC H II region G333.6-0.2. The main results are summarized as follows.

We identified three hot molecular cores, designated A, B, and C, in which all ten observed K components of the $J = 14 \rightarrow 13$ rotational ladder of CH_3CN were detected, along with emission in the CH_3OH line. Rotational diagrams of the methyl cyanide (CH_3CN) emission show excitation temperatures and column densities of 430 $\pm$ 65 K and 2.24×10^{12} cm^{-2} for core A and 383 $\pm$ 46 K and 7.94×10^{12} cm^{-2} for core B.

The first-order moment maps of the CH_3CN and CH_3OH lines show that the molecular gas exhibits two distinct velocity gradients: one from southwest (SW) to northeast (NE), indicating gas expansion, and another from southeast (SE) to northwest (NW), suggesting rotational motion in core A. In addition, velocity gradients were identified in cores B and C: in core B, the gradient is oriented from southeast to northwest and in core C, from west to east. The velocity gradients observed in the first-order moment maps are consistent with rotational motion.The position–velocity analysis confirms differential rotation in all three cores, with core A showing a Keplerian-like profile.

Emission was detected in the H29α line, with a line center velocity of $V_{\rm LSR} = -40.57 \pm 0.05\,\mathrm{km\,s^{-1}}$ and a linewidth (FWHM) of $30.2 \pm 0.12\,\mathrm{km\,s^{-1}}$. The observed linewidth is attributed to dynamical and/or turbulent motions of hot ionized gas, with contributions from dynamical broadening $\Delta V_{\rm dyn} \approx 23.01\,\mathrm{km\,s^{-1}}$, thermal broadening $\Delta V_{\rm ther} \approx 19.56\,\mathrm{km\,s^{-1}}$ and negligible pressure broadening $\Delta V_{\rm P} \approx 0.02$ km s^{-1}. The dominance of dynamical broadening suggests the presence of large-scale motions, further supported by the intensity-weighted velocity map of the H29α line. The He29α line exhibits a central velocity of $V_{\rm LSR} = -37.52 \pm 0.5\,\mathrm{km\,s^{-1}}$.

The radio recombination line indicates that the ionized gas originates from a region with a radius of 0.0053 pc, an ionized gas mass of $(3.9 \pm 2.5) \times 10^{-2}$ $M_\odot$, an emission measure of 1.23×10^9 $\pm$ 5.71×10^6, and an electron density of $(4.8 \pm 0.41) \times 10^5$ cm^{-3}, assuming a distance of 4.2 kpc. We also calculated the Lyman continuum photon flux, which indicates the presence of a massive star with a spectral type of O5$-$O6 V (ZAMS).

We conclude that the physical parameters of the H II region suggest an intermediate evolutionary stage between the HC and UC H II regions.

Author Contributions: Conceptualization , A.O.; methodology, A.O. and A.A.; software, A.O.; validation, A.N., A.N. and M.K.; formal analysis, A.O., A.A. and Z.I.; investigation, A.O., A.M. and A.D.; resources, A.N.; data curation, A.A.; writing—original draft, A.O.; writing—review and editing, N.A. and K.T.; visualization, A.O., A.A. and Z.I. All authors have read and agreed to the published version of the manuscript.

Funding: This research was funded by the Science Committee of the Ministry of Science and Higher Education of the Republic of Kazakhstan (Grant No. AP23489575).

Data Availability Statement: The data used in this study are archival Atacama Large Millimeter/submillimeter Array (ALMA) Band 6 observations, available under project code 2016.1.00577.S from the ALMA Science Archive (accessed on 28 July 2023; https://almascience.eso.org/).

Conflicts of Interest: The authors declare no conflict of interest.

Abbreviations

The following abbreviations are used in this manuscript: HMSFRs—High-mass star-forming regions; ALMA—Atacama Large Millimeter/Submillimeter Array; ISM—Interstellar Medium; RRL—Radio recombination line; ZAMS—Zero Age Main Sequence; COMs—Complex Organic Molecules; UC H II—Ultracompact H II region; HC H II—Hypercompact H II region; CASA—Common Astronomy Software Applications; CARTA—Cube Analysis and Rendering Tool for Astronomy; MADCUBA—Madrid Data Cube Analysis.

References

1. Tan, J.C.; Beltrán, M.T.; Caselli, P.; Fontani, F.; Fuente, A.; Krumholz, M.R.; McKee, C.F.; Stolte, A. Massive Star Formation. In *Protostars and Planets VI*; Beuther, H., Klessen, R.S., Dullemond, C.P., Henning, T., Eds.; University of Arizona Press: Baltimore, MD, USA, 2014; pp. 149–172. [CrossRef]
2. van Dishoeck, E.F.; Blake, G.A. Chemical Evolution of Star-Forming Regions. *Annu. Rev. Astron. Astrophys.* **1998**, *36*, 317–368. [CrossRef] [PubMed]
3. Cesaroni, R.; Hofner, P.; Araya, E.; Kurtz, S. The structure of hot molecular cores over 1000 AU. *Astron. Astrophys.* **2010**, *509*, A50. [CrossRef]
4. Bonfand, M.; Belloche, A.; Menten, K.M.; Garrod, R.T.; Müller, H.S.P. Exploring molecular complexity with ALMA (EMoCA): Detection of three new hot cores in Sagittarius B2(N). *Astron. Astrophys.* **2017**, *604*, A60. [CrossRef]
5. Keto, E.; Wood, K. Observations on the Formation of Massive Stars by Accretion. *Astrophys. J.* **2006**, *637*, 850–859. [CrossRef]
6. Kurtz, S.; Cesaroni, R.; Churchwell, E.; Hofner, P.; Walmsley, C.M. Hot Molecular Cores and the Earliest Phases of High-Mass Star Formation. In *Protostars and Planets IV*; Mannings, V., Boss, A.P., Russell, S.S., Eds.; University of Arizona Press: Baltimore, MD, USA, 2000; pp. 299–326.
7. Goss, W.M.; Shaver, P.A. Galactic Radio Sources I: High Resolution 5000 MHz observations. *Aust. J. Phys. Astrophys. Suppl.* **1970**, *14*, 1.
8. Fujiyoshi, T.; Smith, C.H.; Caswell, J.L.; Moore, T.J.T.; Lumsden, S.L.; Aitken, D.K.; Roche, P.F. Radio and infrared recombination studies of the southern massive star forming region G333.6-0.2. *Mon. Not. R. Astron. Soc.* **2006**, *368*, 1843–1855. [CrossRef]
9. Grave, J.M.C.; Kumar, M.S.N.; Ojha, D.K.; Teixeira, G.D.C.; Pace, G. The ionizing sources of luminous compact HII regions in the RCW106 and RCW122 clouds. *Astron. Astrophys.* **2014**, *563*, A123. [CrossRef]
10. Conti, P.S.; Crowther, P.A. MSX mid-infrared imaging of massive star birth environments - II. Giant HII regions. *Mon. Not. R. Astron. Soc.* **2004**, *355*, 899–917. [CrossRef]
11. Fujiyoshi, T.; Smith, C.H.; Moore, T.J.T.; Aitken, D.K.; Roche, P.F.; Quinn, D.E. 12-μm fine-structure emission line and continuum images of G333.6-0.2. *Mon. Not. R. Astron. Soc.* **1998**, *296*, 225–230. [CrossRef]
12. Kumar, M.S.N. Radiatively driven Rayleigh-Taylor instability candidates around a forming massive star system. NACO adaptive optics and VISIR study of G333.6-0.2. *Astron. Astrophys.* **2013**, *558*, A119. [CrossRef]

13. Mookerjea, B.; Kramer, C.; Nielbock, M.; Nyman, L.Å. The Giant Molecular Cloud associated with RCW 106. A 1.2 mm continuum mapping study. *Astron. Astrophys.* **2004**, *426*, 119–129. [CrossRef]
14. McMullin, J.P.; Waters, B.; Schiebel, D.; Young, W.; Golap, K. CASA Architecture and Applications. In Proceedings of the Astronomical Data Analysis Software and Systems XVI, Tucson, AZ, USA, 15–18 October 2017; Astronomical Society of the Pacific Conference Series; Shaw, R.A., Hill, F., Bell, D.J., Eds.; Astronomical Society of the Pacific: San Francisco, CA, USA, 2007; Volume 376, p. 127.
15. Astropy Collaboration; Robitaille, T.P.; Tollerud, E.J.; Greenfield, P.; Droettboom, M.; Bray, E.; Aldcroft, T.; Davis, M.; Ginsburg, A.; Price-Whelan, A.M.; et al. Astropy: A community Python package for astronomy. *Astron. Astrophys.* **2013**, *558*, A33. [CrossRef]
16. Bonfand, M.; Csengeri, T.; Bontemps, S.; Brouillet, N.; Motte, F.; Louvet, F.; Ginsburg, A.; Cunningham, N.; Galván-Madrid, R.; Herpin, F.; et al. ALMA-IMF. XI. The sample of hot core candidates: A rich population of young high-mass protostars unveiled by the emission of methyl formate. *Astron. Astrophys.* **2024**, *687*, A163. [CrossRef]
17. Csengeri, T.; Bontemps, S.; Wyrowski, F.; Megeath, S.T.; Motte, F.; Sanna, A.; Wienen, M.; Menten, K.M. The ATLASGAL survey: The sample of young massive cluster progenitors. *Astron. Astrophys.* **2017**, *601*, A60. [CrossRef]
18. Motte, F.; Bontemps, S.; Csengeri, T.; Pouteau, Y.; Louvet, F.; Stutz, A.M.; Cunningham, N.; López-Sepulcre, A.; Brouillet, N.; Galván-Madrid, R.; et al. ALMA-IMF. I. Investigating the origin of stellar masses: Introduction to the Large Program and first results. *Astron. Astrophys.* **2022**, *662*, A8. [CrossRef]
19. Komesh, T.; Omar, A.; Garay, G.; Assembay, Z.; Alimgazinova, N.; Zhumabay, N.; Kyzgarina, M. ALMA observations of the environments of G333.0162+00.7615. In Proceedings of the Resolving the Rise and Fall of Star Formation in Galaxies, Busan, Republic of Korea, 9 June 2023; Wong, T., Kim, W.T., Eds.; IAU Symposium; Cambridge University Press: Cambridge, UK, 2023; Volume 373, pp. 35–38. [CrossRef]
20. Assembay, Z.; Komesh, T.; Garay, G.; Omar, A.; Esimbek, J.; Alimgazinova, N.; Kyzgarina, M.; Murat, S. ALMA observations of the environments of G301.1364-00.2249A. In Proceedings of the Cosmic Masers: Proper Motion Toward the Next-Generation Large Projects, Kagoshima, Japan, 20–24 March 2023; Hirota, T.; Imai, H.; Menten, K.; Pihlström, Y., Eds.; IAU Symposium; Cambridge University Press: Cambridge, UK, 2024; Volume 380, pp. 204–206. [CrossRef]
21. Martín, S.; Martín-Pintado, J.; Blanco-Sánchez, C.; Rivilla, V.M.; Rodríguez-Franco, A.; Rico-Villas, F. Spectral Line Identification and Modelling (SLIM) in the MAdrid Data CUBe Analysis (MADCUBA) package. Interactive software for data cube analysis. *Astron. Astrophys.* **2019**, *631*, A159. [CrossRef]
22. Komesh, T.; Garay, G.; Henkel, C.; Omar, A.; Estalella, R.; Assembay, Z.; Li, D.; Guzmán, A.; Esimbek, J.; Huang, J.; et al. Infall Motions in the Hot Core Associated with the Hypercompact H II Region G345.0061+01.794 B. *Astrophys. J.* **2024**, *967*, 15. [CrossRef]
23. Roelfsema, P.R.; Goss, W.M. High resolution radio recombination line observations. *Astron. Astrophys. Rev.* **1992**, *4*, 161–214. [CrossRef]
24. Méndez-Delgado, J.E.; Esteban, C.; García-Rojas, J.; Arellano-Córdova, K.Z.; Valerdi, M. Helium abundances and its radial gradient from the spectra of H II regions and ring nebulae of the Milky Way. *Mon. Not. R. Astron. Soc.* **2020**, *496*, 2726–2742. [CrossRef]
25. Gordon, M.A.; Sorochenko, R.L. *Radio Recombination Lines: Their Physics and Astronomical Applications*; Springer: Berlin/Heidelberg, Germany, 2002; Volume 282. [CrossRef]
26. Wilson, T.L.; Rohlfs, K.; Hüttemeister, S. *Tools of Radio Astronomy*; Springer: Berlin/Heidelberg, Germany, 2009. [CrossRef]
27. Shi, H.; Zhao, J.H.; Han, J.L. Nature of W51e2: Massive Cores at Different Phases of Star Formation. *Astrophys. J.* **2010**, *710*, 843–852. [CrossRef]
28. Manapbayeva, A.; Omar, A.; Alimgazinova, N.; Komesh, T.; Kyzgarina, M.; Esimbek, J.; Assembay, Z. Determination of physical parameters of the W40 HII region using observations of H110α radio recombination line. *Rec. Contr. Phys.* **2023**, *86*, 4–11. [CrossRef]
29. Rubin, R.H. A Discussion of the Sizes and Excitation of H II Regions. *Astrophys. J.* **1968**, *154*, 391. [CrossRef]
30. Mezger, P.G.; Smith, L.F.; Churchwell, E. IR-excess Radiation and the Absorption Characteristics of Dust in Galactic H II Regions. *Astron. Astrophys.* **1974**, *32*, 269.
31. Matsakis, D.N.; Evans, N.J. II; Sato, T.; Zuckerman, B. Radio continuum measurements of compact H II regions and other sources. *Astron. J.* **1976**, *81*, 172–177. [CrossRef]
32. Mehringer, D.M. Radio Continuum and Radio Recombination Line Observations of W51. *Astrophys. J. Suppl.* **1994**, *91*, 713. [CrossRef]

33. Panagia, N. Some Physical parameters of early-type stars. *Astron. J.* **1973**, *78*, 929–934. [CrossRef]
34. Yang, A.Y.; Urquhart, J.S.; Thompson, M.A.; Menten, K.M.; Wyrowski, F.; Brunthaler, A.; Tian, W.W.; Rugel, M.; Yang, X.L.; Yao, S.; et al. A population of hypercompact H II regions identified from young H II regions. *Astron. Astrophys.* **2021**, *645*, A110. [CrossRef]